# BENDING AND VIBRATION ANALYSIS OF MAGNETO-ELECTRO BILATERALLY COATED QUASI-3D MICROBEAM VIA DQ-FEM

Besma KHOUANI\*, Ahmed SAIMI\*\*, Ismail BENSAID\*

"IS2M Laboratory, Mechanical engineering Department, Faculty of Technology, University Abou Beckr Beklaid, Tlemcen, Algeria ""Mechanical engineering Department, Faculty of Science and Technology, University Belhadj Bouchaib, Ain Temouchent, Algeria

besma.khouani@univ-tlemcen.dz, ahmed.saimi@univ-temouchent.edu.dz, ismail.bensaid@univ-tlemcen.dz

received 26 December 2024, revised 09 April 2025, accepted 10 April 2025

Abstract: In this study, the static bending and free vibration of a bilaterally coated magneto electro elastic (MEE) functionally graded (FG) microbeam is analysed by using a high order quasi-3D beam theory, along with a Differential Quadrature Finite Element Method (DQ-FEM). The power formulation for FG gradation through the thickness direction is considered. The microbeam consists of two materials, one possessing piezo-magneto-electric characteristics and the other without them. The material characteristics are progressively graded from the outermost surfaces to the innermost core. In order to localize the microstructural effect of the beam, the modified couple stress theory (MCST) is incorporated. By the application of Lagrange's theorem and Gauss-Lobato node scheme, the general governing equation are established. Through the implementation of the established model, "the static bending and free vibration" analysis are determined. To illustrate the effectiveness and accuracy of this particular numerical resolution method, the obtained results are validated with similar outcomes in existing literature. The effects of the material gradation volume fraction index, and the length-thickness ratio on the natural frequencies and static bending are investigated. The results reveal that the material distribution plays a significant role in influencing both static bending and free vibration behavior. Material composition plays a critical role, with higher proportions of MEE material enhancing the piezoelectric effect and magnetostrictive response, respecting the material gradation with optimized combinations of MEE material for higher deflection and optimal electric and magnetic potentials. This study provides a comprehensive framework for optimizing MEE microbeams in applications requiring precise control of mechanical, electrical, and magnetic responses.

Key words: higher-order Q3D beam theory, magneto-electro-elastic microbeam, MCST, DQ-FEM, FGM

## 1. INTRODUCTION

Magneto-electro-elastic materials have sparked widespread attention due to their multifunctional features, which integrate mechanical, electrical, and magnetic forces. These materials are commonly employed in sophisticated engineering applications such as sensors, actuators, and energy harvesters. Understanding these materials' mechanical behavior, particularly in microbeam structures, is critical for maximizing their performance and dependability in practical applications [1-4]. "In addition, functionally graded materials (FGM) exhibit continuous changes in properties through various direction. FGM offer several benefits, including temperature protection, sound insulation, and energy and electromagnetic wave absorption [5-7]. Currently, scientists have been interested in evaluating the mechanical behavior of laminated-surface- piezoelectric in host structures [8]. Research into multilayer magneto-electroelastic functionally graded materials (MEE-FGMs) on thin beams and plates has gained popularity in recent years. [9] investigated the free vibration behavior of both anisotropic and linear MEE-FGM plates. [10] suggested a meshless approach for analyzing the bending of circular MEE-FGM plates. [11] conducted an inquiry into the implications of porosity on the nonlinear deformation characteristics exhibited by functionally graded magneto-electro-elastic smart shells in the context of simultaneous application of loads. [12] analyzed the static bending and the free vibration of a transversely isotropic magneto-electro-elastic beam including microstructure and foundation effects. [13] studied the bending and vibration of FG MEE Timoshenko Microbeams and added wave propagation analysis [14]. [15] developed a microstructure-dependent anisotropic magneto-electro-elastic Mindlin plate model via a modified couple stress theory. Notably, [16] introduced an isogeometric model to study size-dependent effects in magneto-electro-elastic microbeams. Their work highlights the role of gradient index variations in tailoring MEE responses. Similarly, [17] conducted nonlinear bending analysis on nonlocal MEE laminated nanobeams and emphasized the influence of boundary conditions and external electric/magnetic potentials. The thermal buckling behavior of MEE nanobeams has also been explored by [18] who employed von Kármán's nonlinear equations to examine the impact of temperature gradients and electrical/magnetic fields. Further, [19] investigated the nonlinear vibrations of flexoelectric functionally graded nanoplates under the influence of a magnetic field, demonstrating the importance of electromechanical interactions at the nanoscale. [20] extended this research by analyzing nonlinear deformations of MEE nanobeams resting on an elastic foundation, using a modified couple stress theory to accurately capture nonlocal effects. Additionally, [21] investigated the free vibration characteristics of MEE nanobeams in a thermal environment, revealing the dependency of natural frequencies on length and thickness variations. In the context of buckling analysis, [22] focused on size-dependent magnetoelectromechanical buckling using strain gradient theory, showing how mechanical and electrical fields affect stability conditions. Nonlinear postbuckling behavior has been studied by [23], who analyzed magneto-electro-thermo-elastic laminated microbeams

Bending and Vibration Analysis of Magneto-Electro Bilaterally Coated Quasi-3D Microbeam via DQ-FEM incorporating the modified couple stress theory and Reddy's shear deformation theory. Their results provide key insights into the combined effects of temperature, magneto-electric potential, and slenderness ratio on postbuckling performance. [24] introduced a continuum-based model for functionally graded conical nano/microshells, demonstrating how flexoelectric effects influence static and vibrational behaviors. [25] presented a nonlinear dynamic model for geometrically imperfect functionally graded MEE nanobeams, which is essential for understanding real-world imperfections in nanostructures. Recent models, such as the axially functionally graded (AFG) micro-beam based on strain gradient elasticity theory (RSGET), incorporate size effects and material inhomogeneity to analyze the static and dynamic responses at the microscale [26]. Similarly, isogeometric analysis (IGA) has been applied to magneto-electro-elastic functionally graded microplates, highlighting the impact of microstructure effects on mechanical and electromagnetic behaviors [27]. Additionally, a new IGA model for magneto-electro-elastic curved microbeams, considering size effects and the modified couple stress theory (MCST), offers insights into the bending and vibration behaviors of functionally graded structures [16]. These models are essential for optimizing the performance of micro-sensors, actuators, and other micro-scale devices. "Numerous investigations [28, 29] have demonstrated that thin beams and plates typically display size effects. Classical theories at the micro/nano scale cannot account for non-local interactions of material particles at such small scales due to a lack of material length scale parameters. To anticipate size effects, a variety of theories with extra material properties have been developed, including couple stress theories [30-32], strain gradient theories [33-35]. These concepts were effectively used to generate size-dependent structural models at extremely tiny scales. For example, based on nonlocal theories, a variety of MEE beam and plate models have been created to capture non-local size effects [36-39], in which a non-local medium with long-range material interactions is used. [40] suggested a non-local strain gradient theory that incorporates both non-local and strain gradient effects, and the bending, buckling, and free variation issues of FGM beams have been resolved [41, 42]." "Researchers frequently employ 1st "order shear deformable beam theory", (HSBT) "higher-order shear deformable beam theory", and shear and "normal deformable beam theory", commonly known as Q3D theory. The FSBT is the simplest model, but it necessitates a shear correction factor as it does not fulfil the zero traction boundary criterion at the top and bottom surfaces of the beam [43],[44]. The "HSBT" theories were suggested, that enhanced the "transverse shear stress distribution" and, as a result, removed the need for a "shear correction factor" (SCF) [45]. However, HSBT theories do not take into consideration the usual strain as well as stretch effect, which then becomes highly relevant and should be considered for thick typical FGBs. As a consequence, Q3D theories [46], [47] that take shear and stretching effects into account are created by employing the idea of higher order variation in both transverse and axial displacements". In recent decades, numerical and semi-numerical methods, such as the finite element method (FEM) and the generalized differential quadrature method

(GDQM), have gained popularity for their efficiency, flexibility, and

adaptability in solving differential equations related to structural el-

ements with complex effects, including geometries, shapes, inter-

actions, boundary conditions, and more, with precise results. Since

then, other investigations have been conducted using these numerical approaches. [48] investigated the dynamic behavior of function-

ally graded porous beams sitting on a viscoelastic foundation using

GDQM. Dahmane et.al studied the influence of crack on the

dynamic behavior of bidirectional imperfect FG beams on an elastic basis via FEM. [49] used the DQFEM to investigate the dynamic behavior of on-board shafts. [50] investigated the vibration and buckling characteristics of nano-composite beams reinforced with agglomerated carbon nanotubes using the DQFEM. A combined study between DQFEM and MCST to analyze the dynamic behaviors of microbeams was used in several works [51, 52].

The present paper uses the extended modified couple stress theory to develop a bilaterally coated MEE microbeam model via the refined high order beam theory combined with the DQFEM for the first time to solve the static bending and free vibration.

The proposed bilaterally coated magneto-electro-elastic (MEE) microbeam, analyzed using a quasi-3D beam theory and DQ-FEM, has potential applications in various engineering fields. The unique electromechanical coupling behavior enables its use in microelectromechanical systems (MEMS) such as high-sensitivity sensors, actuators, and vibration-based energy harvesters. In biomedical engineering, it can be employed in micro-pumps, biosensors, and drug delivery systems. Additionally, the tailored functionally graded composition makes it suitable for aerospace applications, including adaptive structures and damping mechanisms. These diverse applications highlight the significance of the proposed model in advancing smart material-based technologies.

## 2. FORMULATION

## 2.1. MEE FG microbeam model

This study considers a microbeam of length L, width b, and thickness h, as shown in figure 1, from which the material characteristics are progressively graded from the outer surfaces to the inner core.

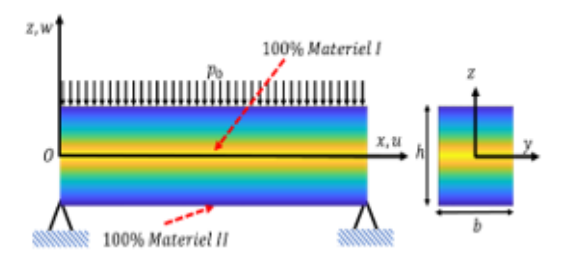


Fig. 1. Piezo- bilaterally FG microbeam model

The material characteristics are considered to change continuously in two opposite direction throughout the thickness (z-axis) based on the power-law distribution [52]. The following equations describe the distribution of material characteristics in FG materials:

$$P(z) = (P_1 - P_2) \left( \left| \frac{|z|}{h} - 1 \right| \right)^{k_z} + P_2$$
 (1)

Where P(z) represent "elastic stiffness, couple stress stiffness, piezoelectric constant, piezomagnetic constant, dielectric constant, magnetic permeability constant, magneto-dielectric constant and density".

The total strain energy in this particular situation is as follow.

$$U = \frac{1}{2} \int_0^L \int_A \left( \sigma_{ij} \varepsilon_{ij} + m_{ij} \chi_{ij} - D_i E_i - B_i H_i \right) dA \, dx \tag{2}$$

The equations representing "transversely isotropic magneto-electro-elastic materials" are provided in accordance with the extended MCST[12]. Where  $\sigma_{ij}$ ,  $m_{ij}$ ,  $D_i$ ,  $B_i$  represent the "Cauchy stress tensor, deviatoric couple stress tensor, electric displacements, and magnetic fluxes:

$$\begin{cases}
\sigma_{xx} \\ \sigma_{zz} \\ \sigma_{zx}
\end{cases} = \begin{bmatrix}
C_{11} & C_{13} & 0 \\ C_{13} & C_{33} & 0 \\ 0 & 0 & C_{55}
\end{bmatrix} \begin{Bmatrix}
\varepsilon_{xx} \\ \varepsilon_{zz} \\ 2\varepsilon_{xz}
\end{Bmatrix} - \begin{bmatrix}
0 & q_{31} \\ 0 & q_{33} \\ q_{15} & 0
\end{bmatrix} \begin{Bmatrix}
H_x \\ H_z
\end{Bmatrix} - \begin{bmatrix}
0 & e_{31} \\ 0 & e_{33} \\ e_{15} & 0
\end{bmatrix} \begin{Bmatrix}
E_x \\ E_z
\end{Bmatrix}$$
(3)

$${ m_{yz} \\ m_{xy} } = \begin{bmatrix} A_{44} & 0 \\ 0 & A_{66} \end{bmatrix} { 2\chi_{yz} \\ 2\chi_{yy} }$$
(4)

$$\begin{cases}
D_{x} \\
D_{z}
\end{cases} = \begin{bmatrix}
0 & 0 & e_{15} \\
e_{31} & e_{33} & 0
\end{bmatrix} \begin{cases}
\varepsilon_{xx} \\
\varepsilon_{zz} \\
2\varepsilon_{zx}
\end{cases} + \begin{bmatrix}
s_{11} & 0 \\
0 & s_{33}
\end{bmatrix} \begin{cases}
E_{x} \\
E_{z}
\end{cases} +$$

$$\begin{bmatrix}
d_{11} & 0 \\
0 & d_{33}
\end{bmatrix} \begin{cases}
H_{x} \\
H_{z}
\end{cases} (5)$$

$$\begin{cases}
B_{x} \\
B_{z}
\end{cases} = \begin{bmatrix}
0 & 0 & q_{15} \\
q_{31} & q_{33} & 0
\end{bmatrix} \begin{cases}
\varepsilon_{xx} \\
\varepsilon_{zz} \\
2\varepsilon_{zx}
\end{cases} + \begin{bmatrix}
\mu_{11} & 0 \\
0 & \mu_{33}
\end{bmatrix} \begin{cases}
H_{x} \\
H_{z}
\end{cases} + \begin{bmatrix}
d_{11} & 0 \\
0 & d_{33}
\end{bmatrix} \begin{cases}
E_{x} \\
E_{z}
\end{cases}$$
(6)

The parameters  $(C_{11}, C_{13}, C_{55})$ ,  $(A_{44}, A_{66})$  describe the elastic stiffness tensor and the couple stress tensor, with:

$$A_{\alpha\beta} = C_{\alpha\beta}l^2 \tag{7}$$

where l is the material length scale parameter (MLSP).

 $q_{i\alpha}, e_{i\alpha}, s_{ij}, \mu_{ij}, d_{ij}$  are the piezomagnetic tensor, the piezoelectric tensor, the dielectric tensor, the magnetic permeability tensor, and the magneto-dielectric tensor respectively. And  $\varepsilon_{ij}, \chi_{xx}$  are "the strain tensor and the rotationally symmetric gradient tensor", which are described by the following equations: [53]

$$\varepsilon_{ij} = \frac{1}{2} \left( u_{i,j} + u_{j,i} \right) \tag{8}$$

$$\chi_{ij}^{s} = \frac{1}{2} \left( \theta_{i,j} + \theta_{j,i} \right) \tag{9}$$

$$\theta_i = \frac{1}{2} e_{ijk} u_{k,j} \tag{10}$$

The variables  $u_i$  and  $\theta_i$  represent the components of the displacement vector and rotation vectors, respectively.  $e_{ijk}$  is the permutation symbol. Also,  $E_i$  and  $H_i$  represent the electric field and magnetic field intensities, respectively. [15]

$$E_i = -\Phi_{,i}$$
 ,  $H_i = -M_{,i}$  (11)

 $\Phi$  and M represent the "electric and magnetic potentials, respectively.

In accordance with the higher order quasi-3D beam theory [50], The current study posits that the field of displacement at any random spot on the microbeam can be expressed as follows:

$$\begin{cases} u(x,z,t) = u_0(x,t) - z\frac{dw_b}{dx} + f(z)\frac{dw_s}{dx} \\ w(x,z,t) = w_b(x,t) + w_s(x,t) + g(z)w_z(x,t) \end{cases}$$
 (12)

The transversal displacement is divided into two components, notably  $w_b$ ,  $w_s$  and  $w_z$ , following this method. Where u,  $w_b$ ,  $w_s$  and  $w_z$  represents the displacement in the x-direction, the bending component, the shear components and the stretching components

of the transverse displacement of the points on the neutral axis of the beam, respectively. The selection of our function f(z) is governed by the shear function provided by Reddy in equation (15).

$$f(z) = z - \left(1 - \left(\frac{4z^2}{3h^2}\right)\right), \ g(z) = \left(1 - \frac{df}{dz}\right)$$
 (13)

The distribution of electric and magnetic potentials in the thickness direction of the piezoelectric inner layer (core) is provided by [13]:

$$\begin{cases} \Phi(x,z,t) = -\cos\left(\frac{\pi}{h}z\right)\gamma(x,t) + \frac{2z}{h}\gamma_0\\ M(x,z,t) = -\cos\left(\frac{\pi}{h}z\right)\zeta(x,t) + \frac{2z}{h}\zeta_0 \end{cases} \tag{14}$$

The spatial variations of electric potential in the x-direction are represented by  $\gamma$ , while the external electric potential is denoted as  $\gamma_0$ .  $\zeta$  and  $\zeta_0$  represent the spatial variations of the magnetic potential in the x-direction and the external magnetic potential, respectively. Several studies used uniform distribution in the longitudinal direction and linear distribution [54, 55]. Works donne by Gopinathan [56] and Wang and Quek [57] demonstrated that a quadratic or half-cosine distribution provides a more accurate representation, as it better satisfies Maxwell's static electricity equation. The electric and megnitic potential distribution we adopted follows this approach. The choice of electric and magnetic potential distributions directly affects the coupling terms in the strain energy expression. A different assumption, such as a purely linear distribution, would result in different governing equations, potentially missing key coupling effects. By considering a half-cosine and linear variation, the proposed model ensures that the strain energy formulation incorporates essential electro-magnetic coupling effects without neglecting significant terms.

By substituting equation (12) into equation (8), the non-zero components of the deformation tensor are extracted as:

$$\begin{cases} \varepsilon_{xx} = \frac{du}{dx} - z \frac{d^2 w_b}{dx^2} - f \frac{d^2 w_s}{dx^2} \\ \varepsilon_{zz} = \frac{dg}{dz} w_z \\ \varepsilon_{xz} = \frac{1}{2} g \left( \frac{dw_s}{dx} + \frac{dw_z}{dx} \right) \end{cases}$$
(15)

Replacing equation (12) into (10) and (9) gives:

$$\begin{cases} \chi_{yz} = \chi_{zy} = -\frac{1}{4} \left( \frac{d^2 f}{dz^2} \frac{dw_s}{dx} + \frac{dg}{dz} \frac{dw_z}{dx} \right) \\ \chi_{xy} = \chi_{yx} = -\frac{1}{4} \left( 2 \frac{d^2 w_b}{dx^2} + \left( \frac{df}{dz} + 1 \right) \frac{d^2 w_s}{dx^2} + g \frac{d^2 w_z}{dx^2} \right) \end{cases}$$
(16)

Introducing equation (14) into (11) yields:

$$\begin{cases} H_{x} = \left(\cos\left(\frac{\pi}{h}z\right)\frac{d\zeta}{dx}\right) \\ H_{z} = \left(-\frac{\pi}{h}\sin\left(\frac{\pi z}{h}\right)\zeta - \frac{2}{h}\zeta_{0}\right) \\ E_{x} = \left(\cos\left(\frac{\pi}{h}z\right)\frac{d\gamma}{dx}\right) \\ E_{z} = \left(-\frac{\pi}{h}\sin\left(\frac{\pi z}{h}\right)\gamma - \frac{2}{h}\gamma_{0}\right) \end{cases}$$

$$(17)$$

Given Equations (8)-(11), the constitutive equation (2) is derived as follows:

 $\{I_{1:6}\}=\int C_{11}(1,z,f,zf,z^2,f^2)dzdy$  ${I_{8:10}} = \int C_{13} \frac{dg}{dz} (1, z, f) dz dy$  $\{I_{12:14}\} = \int e_{31} \frac{\pi}{h} \sin\left(\frac{\pi z}{h}\right) (1, z, f) dz dy$  $\{I_{18:19}\} = \int g \frac{\pi}{h} \cos\left(\frac{\pi z}{h}\right) (e_{15}, q_{15}) dz dy$  $\{I_{22:24}\} = \int \left(\frac{\pi}{h}\cos\left(\frac{\pi z}{h}\right)\right)^2 (s_{11}, \mu_{11}, d_{11}) dz dy$  $\{I_7\} = \int C_{33} \left(\frac{dg}{dz}\right)^2 dz dy, \{I_{11}\} = \int C_{55} g^2 dz dy$  $\{I_{15:17}\} = \int q_{31} \frac{\pi}{h} \sin\left(\frac{\pi z}{h}\right) (1, z, f) dz dy$  $\{I_{20:21}\} = \int \frac{dg}{dz} \frac{\pi}{h} \sin\left(\frac{\pi z}{h}\right) (e_{33}, q_{33}) dz dy$  $\left\{ \{I_{25:27}\} = \int \left(\frac{\pi}{h} \sin\left(\frac{\pi z}{h}\right)\right)^2 (s_{33}, \mu_{33}, d_{33}) dz \, dy \right\}$  $\{D_{1:3}\} = \int \frac{1}{4} A_{44} \left( \left( \frac{d^2 f}{dz^2} \right)^2, \left( \frac{dg}{dz} \right)^2, \frac{d^2 f}{dz^2} \frac{dg}{dz} \right) dz dy$  $\left\{ \{D_{4:9}\} = \int \frac{1}{4} A_{66} \left( 1, \left( \frac{df}{dz} + 1 \right), g, g \left( \frac{df}{dz} + 1 \right), \left( \frac{df}{dz} + 1 \right)^2, g^2 \right) dz dy \right\}$ 

$$\begin{split} U &= \frac{1}{2} \int_{0}^{1} \left( I_{1} \left( \frac{du}{dx} \right)^{2} - 2I_{2} \frac{du}{dx} \frac{d^{2}w_{b}}{dx^{2}} - 2I_{3} \frac{du}{dx} \frac{d^{2}w_{s}}{dx^{2}} + 2I_{4} \frac{d^{2}w_{b}}{dx^{2}} \frac{d^{2}w_{s}}{dx^{2}} + I_{5} \left( \frac{d^{2}w_{b}}{dx^{2}} \right)^{2} + I_{6} \left( \frac{d^{2}w_{s}}{dx^{2}} \right)^{2} + I_{7}w_{z}^{2} + 2I_{8} \frac{du}{dx} w_{z} - 2I_{9} \frac{d^{2}w_{b}}{dx^{2}} w_{z} - 2I_{10} \frac{d^{2}w_{s}}{dx^{2}} w_{z} + I_{11} \left( \left( \frac{dw_{s}}{dx} \right)^{2} + \left( \frac{dw_{z}}{dx} \right)^{2} + 2 \frac{dw_{s}}{dx^{2}} \frac{dw_{z}}{dx} \right) + 2I_{12} \frac{du}{dx} \gamma - 2I_{13} \frac{d^{2}w_{b}}{dx^{2}} \gamma - 2I_{14} \frac{d^{2}w_{s}}{dx^{2}} \gamma + 2I_{15} \frac{du}{dx} \zeta - 2I_{16} \frac{d^{2}w_{b}}{dx^{2}} \zeta - 2I_{17} \frac{d^{2}w_{s}}{dx^{2}} \zeta - 2I_{18} \left( \frac{dw_{s}}{dx} \frac{d\gamma}{dx} - \frac{dw_{z}}{dx} \frac{d\gamma}{dx} \right) - 2I_{19} \left( \frac{dw_{s}}{dx} \frac{d\zeta}{dx} - \frac{dw_{z}}{dx} \frac{d\zeta}{dx} \right) + 2I_{20}w_{z}\gamma + 2I_{21}w_{z}\zeta - I_{22} \left( \frac{d\gamma}{dx} \right)^{2} - I_{23} \left( \frac{d\zeta}{dx} \right)^{2} - 2I_{24} \frac{d\zeta}{dx} \frac{d\gamma}{dx} - I_{25}\gamma^{2} - I_{26}\zeta^{2} - 2I_{27}\gamma\zeta + D_{1} \left( \frac{dw_{s}}{dx} \right)^{2} + D_{2} \left( \frac{dw_{z}}{dx} \right)^{2} + 2D_{3} \frac{dw_{s}}{dx} \frac{dw_{z}}{dx} + 4D_{4} \left( \frac{d^{2}w_{b}}{dx^{2}} \right)^{2} + 4D_{5} \frac{d^{2}w_{b}}{dx^{2}} \frac{d^{2}w_{s}}{dx^{2}} + 2D_{7} \frac{d^{2}w_{s}}{dx^{2}} \frac{d^{2}w_{z}}{dx^{2}} + D_{8} \left( \frac{d^{2}w_{s}}{dx^{2}} \right)^{2} + D_{9} \left( \frac{d^{2}w_{z}}{dx^{2}} \right)^{2} \right) dx \end{split}$$

The Kinetic Energy can be written as:

$$T = \frac{1}{2} \int_{0}^{l} \left[ J_{1} (\dot{u}^{2} + \dot{w}_{b}^{2} + \dot{w}_{s}^{2} + 2\dot{w}_{b}\dot{w}_{s}) - 2J_{2}\dot{u}\frac{d\dot{w}_{b}}{dx} - 2J_{3}\dot{u}\frac{d\dot{w}_{s}}{dx} + 2J_{4}\frac{d\dot{w}_{b}}{dx}\frac{d\dot{w}_{s}}{dx} + J_{5}\left(\frac{d\dot{w}_{b}}{dx}\right)^{2} + J_{6}\left(\frac{d\dot{w}_{s}}{dx}\right)^{2} + J_{7}\dot{w}_{z}^{2} + 2J_{8}(\dot{w}_{b}\dot{w}_{z} + \dot{w}_{s}\dot{w}_{z})\right] dx \tag{21}$$
 with:

$$\{J_1, J_2, J_3, J_4, J_5, J_6, J_7, J_8\} = \int \rho(1, z, f, zf, z^2, f^2, g^2, g) dz dy$$
(22)

Furthermore, the virtual work performed by the applied loades acting on the current quasi-3D microbeam can be written as:

$$\int_{0}^{L} \left[ q_{0} \left( w_{b}(x,t) + w_{s}(x,t) + g(z) w_{z}(x,t) \right) \right] dx \tag{23}$$

## 3. DQ-FEM

This approach combines the "generalized differential quadrature method" (GDQM) with the traditional finite element method (FEM).

In order to simulate our beam, we assume that the shape functions take the following form: [49]

$$q[x] = \sum_{i=1}^{N} L_i(x)q_i \tag{24}$$

With  $L_i$  is the Lagrange polynomial,  $q_i = q(x_i)$ , q = $u, w_b, w_s, w_z, \gamma, \zeta$  are the displacements the spatial variations of the electric potential and  $\zeta_i = \zeta(x_i)$  the spatial variations of the magnetic potential of the Gauss Lobato quadrature points where the nodal displacements DQ of the finite element of the beam.

The derivative of order n at a discrete point  $x_i$  of a field variable f (x) is expressed by": [49]

$$\frac{\partial^{n} F(x,t)}{\partial x^{n}}\Big|_{x_{i}} = \sum_{j=1}^{N} A_{ij}^{(n)} F(x_{j},t) \quad (i = 1,2,3,....,N)$$
 (25)

Where A<sub>ii</sub><sup>(n)</sup> is the weighting coefficient, which is related to the derivative of order n. "The Gaussian - Lobato quadrature rule with a degree of precision (2n-3) for the function F(x) defined in the interval [-1, 1] is:" [49]

$$\int_{-1}^{1} F(x) dx = \sum_{j=1}^{N} C_j F(x_j)$$
 (26)

 $C_{\scriptscriptstyle i}$  is the weighting coefficient of Gauss-Lobatto integration: [58]

$$C_1 = C_N = \frac{2}{N(N-1)},$$

$$C_j = \frac{2}{N(N-1)[P_{N-1}(x_j)]^2} \quad (j \neq 1, N)$$
(27)

x<sub>i</sub> represents the (j-1) zero of the first derivative of Legendre polynomials  $P_{N-1}(x)$ . To achieve rapid convergence and high accuracy, a denser population near the boundaries is essential. Sampling points are selected based on the distribution of the grid of Gauss-Lobato nodes.

$$x_j = -\cos\left(\frac{j-1}{N-1}\pi\right) \tag{28}$$

Gauss-Lobatto nodes are determined using the Newton-Raphson iteration method. The relationship between u and  $\bar{u}$ , as well as , w and  $\overline{w}$ , is established according to rule DQ

$$u=Q\bar{u},~w_b=Q\bar{w}_b,~w_s=Q\bar{w}_s,~\gamma=Q\bar{\gamma},~\zeta=Q\bar{\zeta}$$
 (29) where

$$Q = \begin{bmatrix} 1 & 0 & 0 & \cdots & 0 & 0 \\ A_{1,1}^{(1)} & A_{1,2}^{(1)} & A_{1,3}^{(1)} & \cdots & A_{1,N-1}^{(1)} & A_{1,N}^{(1)} \\ 0 & 0 & 1 & \cdots & 0 & 0 \\ \vdots & \vdots & \vdots & \ddots & \vdots & \vdots \\ 0 & 0 & 0 & \cdots & 0 & 1 \\ A_{N,1}^{(1)} & A_{N,2}^{(1)} & A_{N,3}^{(1)} & \cdots & A_{N,N-1}^{(1)} & A_{N,N}^{(1)} \end{bmatrix}$$
(30)

Utilizing the DQ-FEM, the principles of motion are derived by substituting equations (24-30) into the energy equations (18, 21). Subsequently, by substituting the resulting expressions and applying Lagrange's principle, the following system of equations is obtained. The elementary mass and stiffness matrixs and external loads vector derived using DQ-FEM.

$$[M^e] = \begin{bmatrix} [M^e]_{11} & [M^e]_{12} & [M^e]_{13} & [0] & [0] & [0] \\ & [M^e]_{22} & [M^e]_{23} & [M^e]_{24} & [0] & [0] \\ & & [M^e]_{33} & [M^e]_{34} & [0] & [0] \\ & & [M^e]_{44} & [0] & [0] \\ sym & & & [0] \end{bmatrix}$$
(31)

$$[K^{e}] = \begin{bmatrix} [K^{e}]_{11} & [K^{e}]_{12} & [K^{e}]_{13} & [K^{e}]_{14} & [K^{e}]_{15} & [K^{e}]_{16} \\ & [K^{e}]_{22} & [K^{e}]_{23} & [K^{e}]_{24} & [K^{e}]_{25} & [K^{e}]_{26} \\ & [K^{e}]_{33} & [K^{e}]_{34} & [K^{e}]_{35} & [K^{e}]_{36} \\ & [K^{e}]_{44} & [K^{e}]_{45} & [K^{e}]_{46} \\ sym & [K^{e}]_{55} & [K^{e}]_{56} \end{bmatrix}$$

$$(32)$$

$$[F] = \begin{cases} \begin{bmatrix} 0 \\ [F^e]_{22} \\ [F^e]_{33} \\ [F^e]_{44} \\ [0] \\ [0] \end{bmatrix}$$
 (33)

Hence the components of the elementary stiffness matrice and mass matrix are detailed in the appendix. The "matrices for the whole system are derived applying the MEF principles for constructing elementary matrices,

$$([K] - \omega^2[M])(\bar{u} \quad \bar{w}_b \quad \bar{w}_s \quad \bar{w}_z \quad \bar{\gamma} \quad \bar{\zeta})^{\mathrm{T}} = \{F\}$$
 (34)

Since the Differential Quadrature Finite Element Method (DQFEM) follows a similar approach to the Finite Element Method (FEM), the electrical and magnetic boundary conditions are applied in the same manner as the displacement boundary conditions. Specifically, for clamped (C), simply supported (S), and free (F) beams, the electric and magnetic boundary conditions. At clamped and simply supported ends the electrical potential  $\gamma=0$  and also the magnitic potential  $\zeta=0$ .

In the Differential Quadrature Finite Element Method (DQFEM), boundary conditions are imposed by modifying the elementary matrices through the elimination of specific rows and columns associated with the constrained generalized coordinates. For the Simply Supported Case: The first and penultimate rows and columns are eliminated from the elementary matrices to enforce the boundary conditions. This ensures that the displacement at the supports is constrained while allowing rotation. For Clamped (Fixed) Case: The first, second, penultimate, and last rows and columns are eliminated. This fully constrains both displacement and rotational degrees of freedom, ensuring a rigid connection at the clamped boundary. This approach effectively reduces the system's degrees of freedom, ensuring that the boundary conditions are properly enforced in the numerical model while maintaining accuracy and stability in the solution process.

Numerical results and validation

In this work, the  ${\rm BaTiO_3-CoFe_2O_4}$  [12, 15, 59] is chosen as inner core material (Table 1). For the upper and bottom outer surfaces, epoxy [60] is used, from which this mixture is controlled by the power law of FG materials in equation (1). The physical characteristics of these materials are listed in Table 1. A uniform continuous load  $q_0=1/2000h\,N/m$  is applied along the microbeam along the Oz axis. In the first step, a comparison with literature works is made, where the model used is a simply supported (S-S) microbeam assumed to be composed of 50%-50%  ${\rm BaTiO_3-CoFe_2O_4}$  [12]. The shape cross section is taken as b=2h and L=20h, and  $h=14.42~\mu m$ . In the second step, a parametrical study is elaborated to observe the behavior of the static bending and the free vibration with different geometrical parameters, and various upper and bottom outer surfaces materials.

The units in table 1 are as follow: the piezoelectric constants are given in  $e_{ij}$  ( $C/m^2$ ), the dielectric constants are given in  $s_{ij}$  ( $10^{-9}C^2/(N.m^2)$ ), the piezomagnetic constants are given in  $q_{ij}$  (N/(A.m)), the magnetoelectric constants are given in  $d_{ij}$  ( $10^{-12}Ns/(V.C)$ ), the magnetic constants are given in  $\mu_{ij}$  ( $10^{-6}Ns^2/C^2$ ), and the density is given in  $\rho(kg/m^3)$ . The material length scale parameter is given in l ( $\mu m$ ).

To validate our model, we computed the semi-analytical model presented in reference [12] and compared it with our method. As shown in Figures 2-4, the results of our current model closely align in midspan with the semi-analytical results from [12]. Our model give the exact shape of the bending , electrical potential and magnetic potential, on the other hand the literature semi analytical model give only the sinusoidal midspan value shape. This comparison supports the validity of the existing model and demonstrates that the DQFEM, in conjunction with the refined high-order beam theory, provides more accurate results at all locations, in contrast to analytical methods, which only provide data at the midline. Table 2 presents a comparison of the first and second frequencies, as well as the midspan deflection, electric potential, and magnetic potential. The results in Table 2 further confirm the effectiveness and validity of our model.

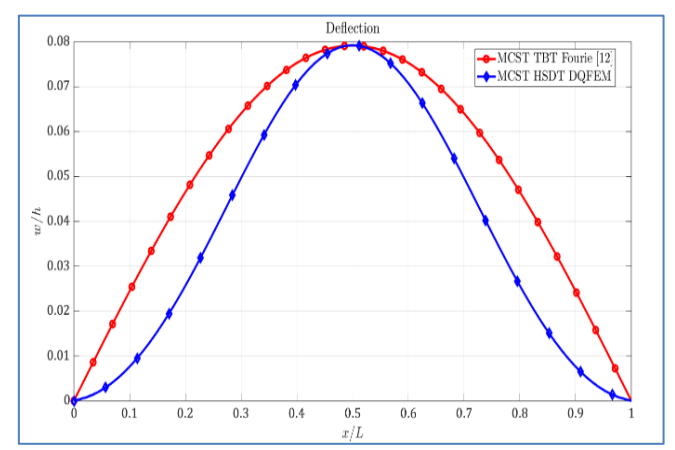


Fig. 2. Comparative analysis of the bending of a doubly S-S microbeam exposed to an even distribution of load

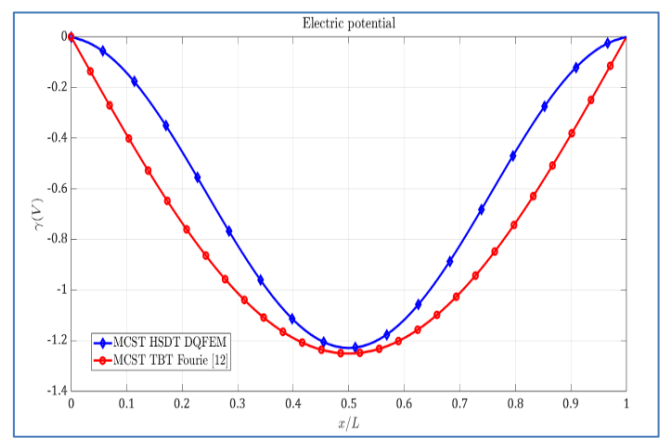


Fig. 3. Comparative analysis of electrical potential of a doubly S-S microbeam exposed to an even distribution of load



**Tab. 1.** Materials Properties of the mixture  $(BaTiO_3 - CoFe_2O_4)$ 

	BaTiO <sub>3</sub> - CoFe <sub>2</sub> O <sub>4</sub>								
	0%-100%	20%-80%	40%-60%	50%-50%	60%-40%	80%-20%	100%-0%	epoxy	
$C_{11}$	286	262	238	226	214	190	166	4.889	
$C_{13}$	170	151.6	133.2	124	114.8	96.4	78	2.407	
$C_{33}$	269.5	248	226.5	215.75	205	183.5	162	4.889	
$C_{55}$	45.3	44.84	44.38	44.15	43.92	43.46	43	1.241	
$q_{31}$	580.3	464.24	348.18	290.15	232.12	116.06	0	0	
$q_{33}$	699.7	559.76	419.82	349.85	279.88	139.94	0	0	
$q_{15}$	550	440	330	275	220	110	0	0	
$e_{31}$	0	-0.88	-1.76	-2.2	-2.64	-3.52	-4.4	0	
$e_{33}$	0	3.72	7.44	9.3	11.16	14.88	18.6	0	
$e_{15}$	0	2.32	4.64	5.8	6.96	9.28	11.6	0	
S <sub>11</sub>	0.08	2.3	4.53	5.64	6.75	8.98	11.2	0	
S <sub>33</sub>	0.093	2.59	5.10	6.35	7.6	10.10	12.6	0	
$d_{11}$	0	2.6	4.58	5.38	6.02	7.04	0	0	
$d_{33}$	0	2020	2760	2740	2520	1550	0	0	
$\mu_{11}$	590	473	356	297.5	239	122	5	0	
$\mu_{33}$	157	127.6	98	83.5	68.8	39.4	10	0	
ρ	5300	5400	5500	5550	5600	5700	5800	1180	
MLSP l	7.33	7.29	7.24	7.21	7.18	7.10	7	16.93	

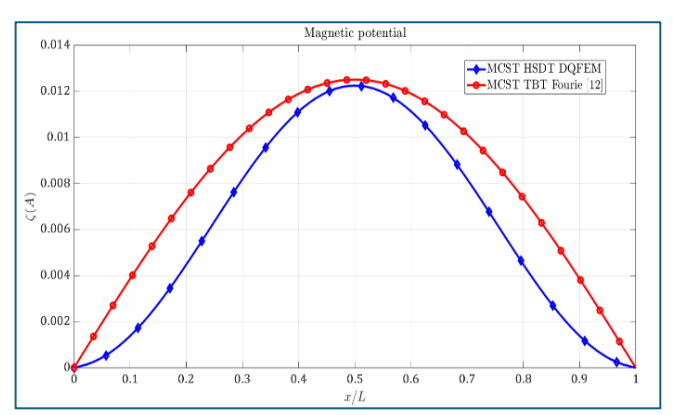
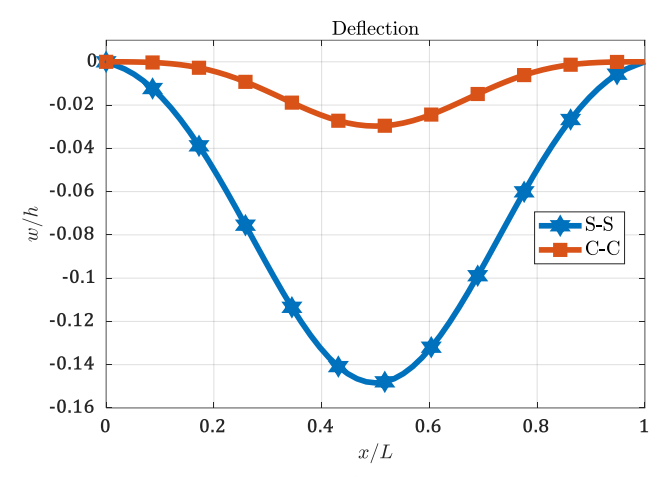


Fig. 4. Comparative analysis of magnetic potential of a doubly S-S microbeam exposed to an even distribution of load

Frequency (MHz)

**Tab. 2.** Comparison of numerical results (b=2h, L=20h), 50%-50% BaTiO $_3$  — CoFe $_2$ O $_4$ 

h(µm)	1st		2 <sup>nd</sup> mode				3 <sup>rd</sup> mode			
	[12]	present	[1:	2]	presen t		[1	2]	presen t	
14.42	4.097	4.069	16.8	311	16.228		39. 7	64	34.853	
28.84	1.710	1.701	7.0	07	6.784		16.		14.796	
h(μm)	Mid: Defle <i>w</i>	Midspan Electric potential $\gamma(V)$			Midspan Magnetic potential $\zeta(A)$					
	[12]	presen t	[12]	presen t		[1	2]	present		
14.42	0.079 2	0.0793	- 1.25 1	-1.2	229	0.0	125	0.0122		
28.84	0.028 4	0.0283	- 0.89 6	-0.8	377	0.00	090	0.0087		



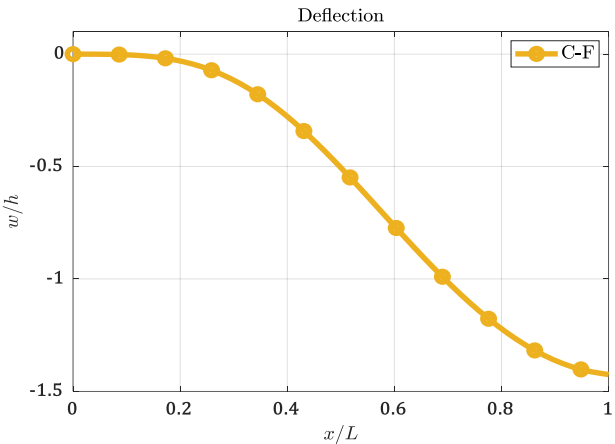
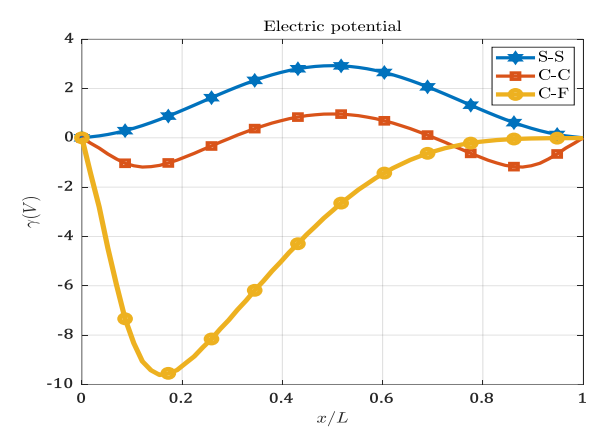


Fig. 5. Deflection of MEE bilaterally microbeam with various boundary conditions  $(k_z=1,\ h=20\mu m,\ b=2h,\ L=20h,\ BaTiO_3(50\%)-CoFe_2O_4(50\%))$ 





**Fig. 6.** Electric potential of MEE bilaterally microbeam with various boundary conditions ( $k_z=1$ ,  $h=20\mu m$ , b=2h, L=20h, BaTiO<sub>3</sub>(50%) – CoFe<sub>2</sub>O<sub>4</sub>(50%))

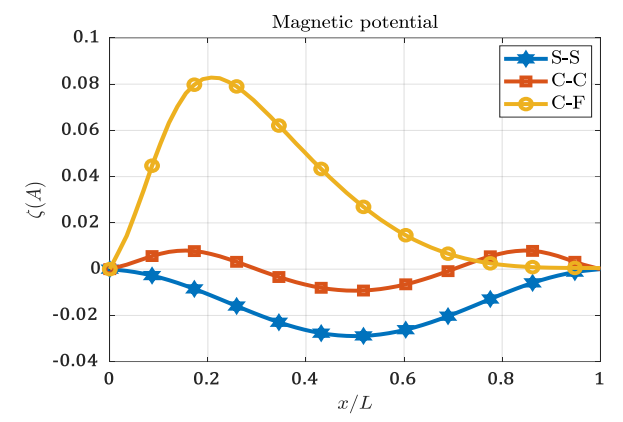


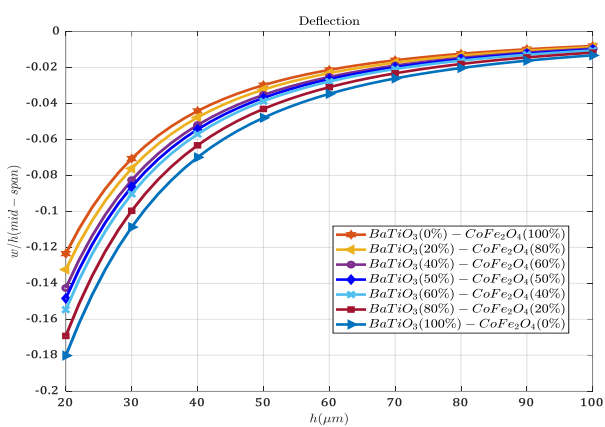
Fig. 7. Magnetic potential of MEE bilaterally microbeam with various boundary conditions  $(k_z = 1, h = 20\mu m, b = 2h, L = 20h$ , BaTiO<sub>3</sub>(50%) – CoFe<sub>2</sub>O<sub>4</sub>(50%))

In Figure 5, we demonstrated the bending response of the magneto-electro-elastic (MEE) bilaterally supported microbeam under different boundary conditions (simply supported, clamped, and clamped-free). The observed variations in deflection arise due to differences in constraint stiffness. The simply supported beam experiences the highest deflection as it lacks rotational constraints at the ends, whereas the clamped beam exhibits reduced deflection due to restricted end rotations.

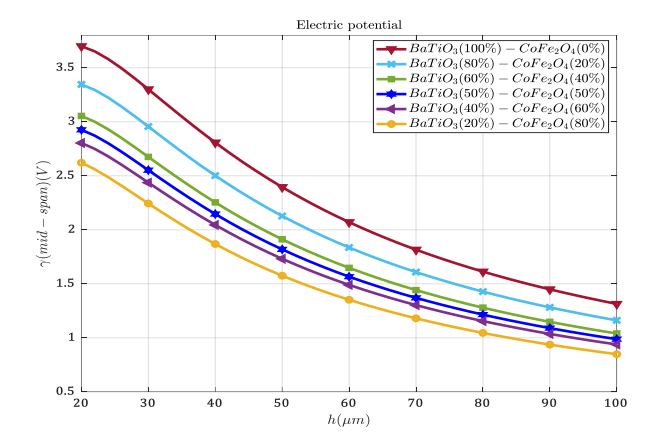
The clamped-free (cantilever) configuration shows the highest deflection at the free end due to the absence of support at one end. This deflection pattern influences the distribution of electric and magnetic potentials along the beam length, as illustrated in Figures 6 and 7.

The electromechanical coupling in the system arises due to the piezoelectric and piezomagnetic effects. When the beam undergoes bending, the induced strain leads to charge polarization. The regions experiencing compression generate a positive electric charge (due to the direct piezoelectric effect) and a negative magnetic charge (due to the piezomagnetic effect), whereas the tensioned regions exhibit the opposite effect.

This explains why, in the simply supported case, the electric potential (V) is uniformly positive (Figures 6), while in the clamped-free case, it is uniformly negative. The clamped configuration results in a more complex charge distribution due to localized constraint effects at the boundaries.



**Fig. 8.** Simply supported microbeam midspan deflection with various thickness and MEE inner material mixture percentage  ${\rm BaTiO_3-CoFe_2O_4}$  ( $k_z=1$ , b=2h, L=20h, )



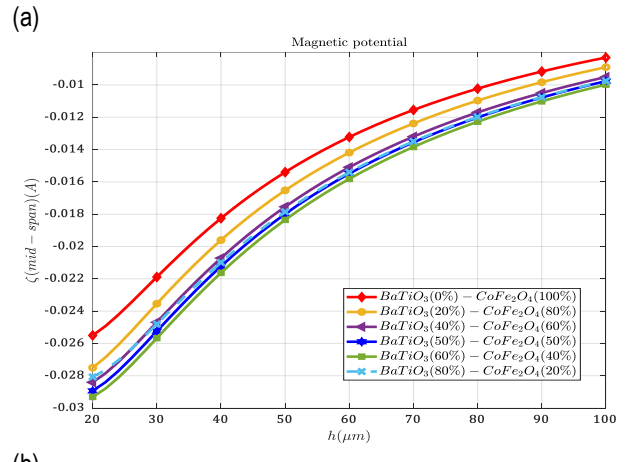
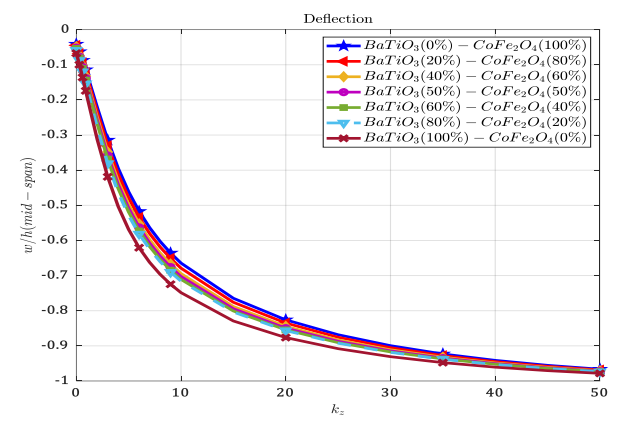


Fig. 9. Electric (a) and magnetic (b) potentials at simply supported microbeam midspan with various thickness and MEE inner material mixture percentage  $BaTiO_3 - CoFe_2O_4$  ( $k_z = 1, \ b = 2h, \ L = 20h,$ )

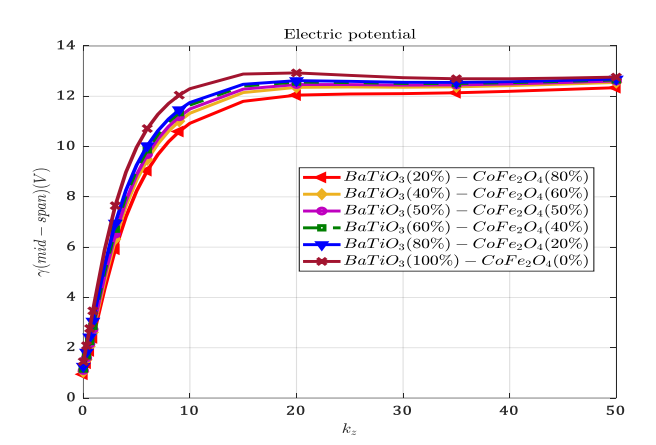
Figures 8 and 9 illustrate the midspan deflection, electric potential, and magnetic potential as functions of beam thickness and inner material composition. The inverse relationship between thickness and deflection is expected, as thicker beams possess higher flexural rigidity, making them more resistant to deformation under the same applied load. Regarding electromechanical behavior, increasing the proportion of BaTiO<sub>3</sub> enhances the piezoelectric response, leading to higher electric potential generation. This occurs because BaTiO<sub>3</sub> is a piezoelectric ceramic with a high electromechanical coupling coefficient, meaning it efficiently converts



mechanical deformation into electrical energy. Conversely,  ${\rm CoFe_2O_4}$  exhibits strong piezomagnetic properties, leading to higher magnetic potential generation. However, as the beam thickness increases, both electric and magnetic potentials decrease because strain distribution becomes more uniform, reducing localized stress concentrations that drive charge generation. This behavior aligns with the fundamental principles of piezoelectric and piezomagnetic materials, where mechanical strain directly affects charge separation and potential generation.



**Fig. 10.** Simply supported microbeam midspan deflection with various FG fraction index and MEE inner material mixture percentage  $BaTiO_3 - CoFe_2O_4$  ( $h = 20\mu m, \ b = 2h, \ L = 20h,$ )



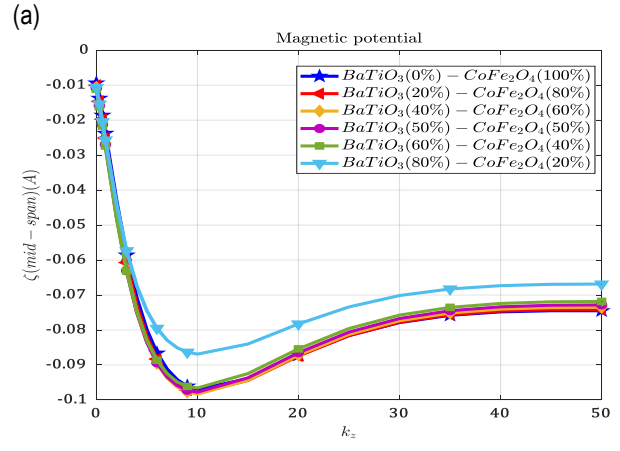
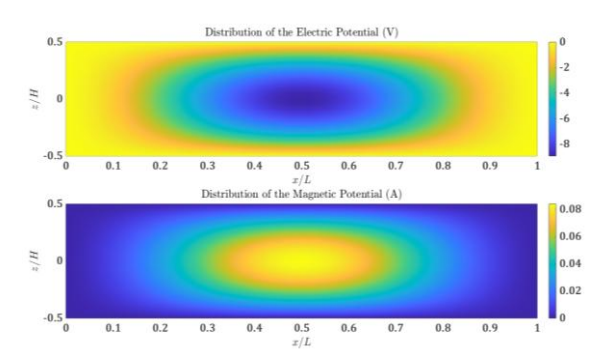


Fig. 11. Electric (a) and magnetic (b) potentials at simply supported microbeam midspan with various FG fraction index and MEE inner material mixture percentage  $BaTiO_3 - CoFe_2O_4$  ( $h = 20\mu m, \ b = 2h, \ L = 20h,$ )

Figures 10 and 11 depict the influence of the functionally graded (FG) material gradation index on the midspan deflection and electromechanical potentials. As the gradation index  $k_z$  increases, the beam composition transitions from a fully magneto-electro-elastic core (BaTiO $_3$  — CoFe $_2$ O $_4$ ) to an outer epoxy-rich composition. Given that epoxy is significantly more flexible and less dense than the ceramic phases, the beam exhibits increased deflection due to reduced overall stiffness.

The electrical and magnetic potentials initially increase with the FG index, peaking at a critical range ( $k_z=[6:20]$ ), before stabilizing. This behavior suggests that an optimal material gradation exists where electromechanical efficiency is maximized. The increasing deflection enhances charge generation up to a certain threshold, beyond which further material gradation reduces effective coupling due to the dominance of the epoxy phase. This insight is crucial for optimizing FG microbeam designs to balance mechanical flexibility and electromechanical efficiency.



**Fig. 12.** Electric and magnetic potentials distribution of simply supported microbeam with  $k_z = 5$ ,  $h = 20\mu m$ , b = 2h, L = 20h, BaTiO<sub>3</sub>(50%) - CoFe<sub>2</sub>O<sub>4</sub>(50%)

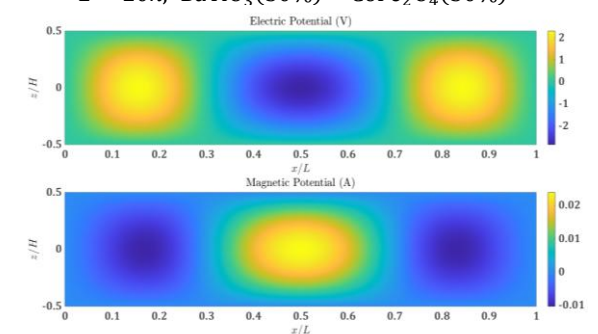


**Fig. 13.** Electric and magnetic potentials distribution of clamped microbeam with  $k_z=5$ ,  $h=20\mu m$ , b=2h, L=20h, BaTiO<sub>3</sub>(50%) - CoFe<sub>2</sub>O<sub>4</sub>(50%)

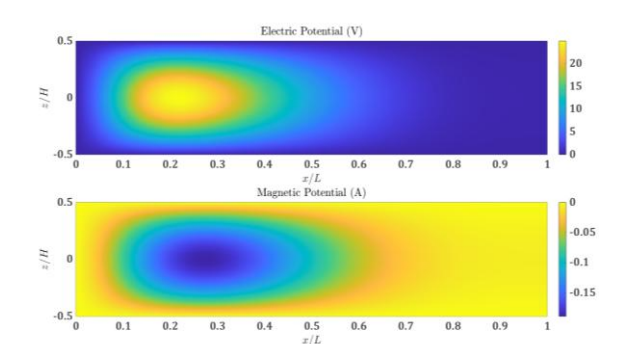


**Fig. 14.** Electric and magnetic potentials distribution of clamped free microbeam with  $k_z=5$ ,  $h=20\mu m$ , b=2h, L=20h, BaTiO<sub>3</sub>(50%) - CoFe<sub>2</sub>O<sub>4</sub>(50%)

Figures 12-14 illustrate the distribution of electric and magnetic potentials across the xOz surface of a magneto-electro-elastic microbeam under different boundary conditions: simply supported (Figure 12), clamped (Figure 13), and clamped-free (Figure 14).

It is evident that the electric and magnetic potential distributions for the simply supported (Figure 12) and clamped (Figure 13) beams exhibit central symmetry.

For the simply supported beam, the maximum values of both electric and magnetic potentials occur at the center. In contrast, for the clamped beam, the highest potentials are found at three locations: near the embedding points and in the center.

In the case of the clamped-free beam, the electric and magnetic potentials are primarily concentrated near the embedding location. In conclusion, the high values of electric and magnetic potentials correspond to areas where bending-induced deformations are most significant.

Figures 15-18 presents the variations in deflection, electrical potential, magnetic potential, and natural frequency respectively for different microbeam thicknesses, considering the length-to-thickness ratio in both the current (MCST) and classical models.

With  $BaTiO_3(50\%) - CoFe_2O_4(50\%)$ . In the numerical analysis, the current model accounts for the couple stress effect, which is incorporated using the Modified Length Scale Parameter (MLSP)  $l \neq 0$  (as defined in Equation (7)).

Conversely, the classical model is derived using the same governing equation but with l=0, meaning that it does not consider the microstructural effects introduced by MCST.

The results indicate that the deflection, electrical potential, and magnetic potential predicted by the current model are consistently lower than those obtained using the classical model across all tested cases.

This discrepancy arises due to the inclusion of the couple stress effect in the MCST model, which introduces additional material stiffness at the microscale. As expected, the difference between the two models becomes more pronounced as the microbeam thickness decreases.

This behavior is due to the fact that size-dependent effects become more significant at smaller scales, where the influence of microstructural mechanics cannot be neglected.

In other words, the classical model, which disregards these effects, tends to overestimate the response of the microbeam in comparison to the MCST-based model.

The increasing stiffness introduced by the couple stress theory results in reduced deflection and altered electrical/magnetic responses, as well as higher natural frequencies.

Additionally, it is observed that as the length-to-thickness ratio increases, the microbeam becomes more flexible, leading to a greater deflection. This increase in deflection consequently enhances both the electrical and magnetic potentials.

On the other hand, the natural frequencies exhibit an inverse relationship with the length-to-thickness ratio, decreasing as the microbeam becomes thinner.

This trend is attributed to the reduced stiffness associated with higher length-to-thickness ratios, which lowers the beam's resistance to dynamic vibrations.

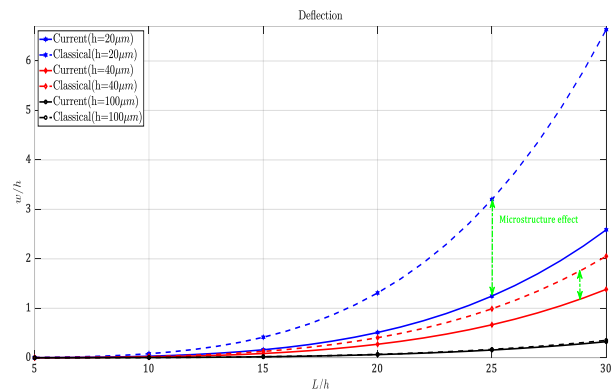


**Fig. 15.** Deflection with respect to length-thickness ratio of simply supported microbeam with  $k_z = 5$ , b = 2h

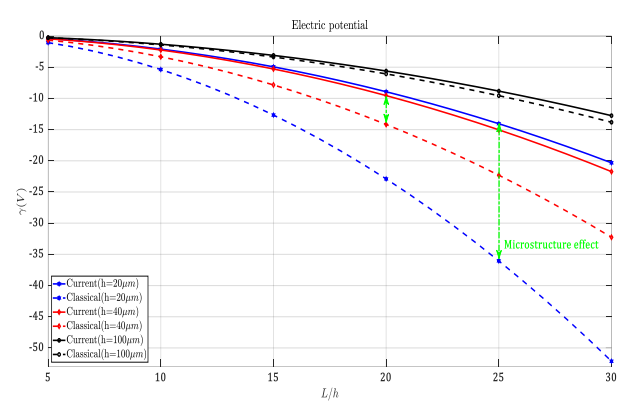
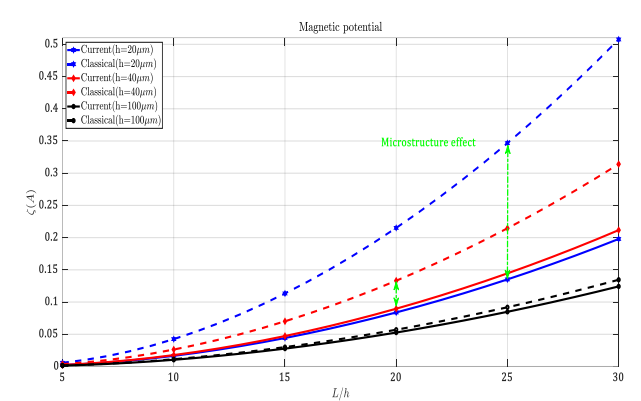


Fig. 16. Electric potential with respect to length-thickness ratio of simply supported microbeam with  $k_z = 5$ , b = 2h



**Fig. 17.** Magnetic potential with respect to length-thickness ratio of simply supported microbeam with  $k_z = 5$ , b = 2h

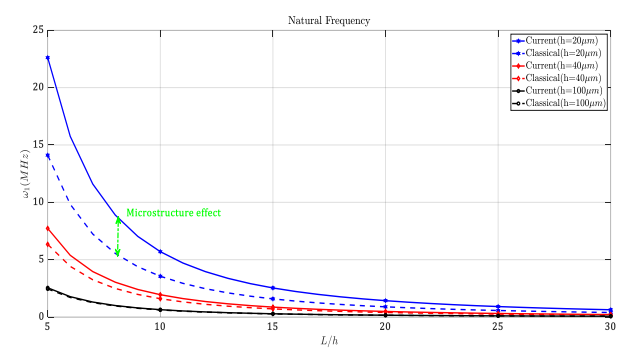


Fig. 18. Natural frequencies with respect to length-thickness ratio of simply supported microbeam with  $k_z=5, b=2h$ 

sciendo

Bending and Vibration Analysis of Magneto-Electro Bilaterally Coated Quasi-3D Microbeam via DQ-FEM

**Tab. 3.** Natural frequency (MHz) of simply supported MEE FG microbeam (b = 2h, L = 20h,)

		$BaTiO_3 - CoFe_2O_4$									
h(µm)	$k_z$	0%-100%	20%-80%	40%-60%	50%-50%	60%-40%	80%-20%	100%-0%			
	0	3.0009	2.8571	2.7108	2.6363	2.5613	2.4071	2.2472			
	0.5	2.5250	2.4124	2.2975	2.2391	2.1802	2.0589	1.9332			
	1	2.2200	2.1283	2.0348	1.9872	1.9393	1.8404	1.7380			
20	5	1.5182	1.4840	1.4491	1.4313	1.4135	1.3766	1.3386			
	10	1.3919	1.3731	1.3539	1.3441	1.3344	1.3141	1.2932			
	15	1.3538	1.3411	1.3282	1.3216	1.3150	1.3013	1.2872			
	20	1.3352	1.3260	1.3166	1.3118	1.3070	1.2970	1.2867			
	0	1.3578	1.2891	1.2191	1.1836	1.1476	1.0739	0.9974			
	0.5	1.0979	1.0449	0.9909	0.9634	0.9356	0.8786	0.8194			
	1	0.9270	0.8847	0.8415	0.8196	0.7973	0.7518	0.7045			
40	5	0.5204	0.5078	0.4950	0.4885	0.4820	0.4687	0.4550			
	10	0.4603	0.4548	0.4492	0.4464	0.4436	0.4378	0.4318			
	15	0.4502	0.4469	0.4435	0.4418	0.4401	0.4366	0.4330			
	20	0.4481	0.4458	0.4435	0.4423	0.4411	0.4387	0.4362			
100	0	0.5260	0.4989	0.4713	0.4572	0.4430	0.4139	0.3836			
	0.5	0.4189	0.3980	0.3768	0.3660	0.3550	0.3326	0.3092			
	1	0.3475	0.3310	0.3141	0.3055	0.2968	0.2789	0.2604			
	5	0.1722	0.1677	0.1633	0.1610	0.1587	0.1541	0.1494			
	10	0.1473	0.1458	0.1442	0.1434	0.1427	0.1411	0.1395			
	15	0.1449	0.1441	0.1433	0.1429	0.1425	0.1417	0.1408			
	20	0.1455	0.1450	0.1445	0.1442	0.1440	0.1434	0.1429			

Table 3 shows the natural frequencies of a simply supported magneto-electro functionally graded microbeam made of BaTiO<sub>3</sub> - CoFe<sub>2</sub>O<sub>4</sub> and epoxy composite material. Here, natural frequencies are influenced by the thickness  $h(\mu m)$  and the powerlaw compositional gradient index  $k_z$ , with different percentages of  $BaTiO_3$  and  $CoFe_2O_4$ . As the thickness  $h(\mu m)$  increases from 20 µm to 100 µm, the natural frequencies decrease across all material distributions and power-law indices. This is expected as thicker beams generally have lower resonant frequencies due to increased mass and flexibility. The material BaTiO<sub>3</sub> - CoFe<sub>2</sub>O<sub>4</sub> distribution percentages (ranging from 0%-100% to 100%-0%) also impact the natural frequencies. Generally, as the proportion of BaTiO<sub>3</sub> increases, the natural frequency decreases. For instance, at  $h=20\mu m$  and  $k_z=0$ , the natural frequency changes from 3.0009 MHz (0%-100%) to 2.2472 MHz (100%-0%). This suggests that a higher content of BaTiO<sub>3</sub> (0%-100%) corresponds to higher stiffness and thus higher natural frequency, while increasing CoFe<sub>2</sub>O<sub>4</sub> content (100%-0%) reduces the stiffness, lowering the natural frequency. For each thickness  $h(\mu m)$ , as  $k_z$  increases from 0 to 20, there is a notable decline in natural frequency, regardless of the  $BaTiO_3 - CoFe_2O_4$  distribution. For instance, at h = $20\mu m$ , with a 0%-100% distribution, natural frequency decreases from 3.0009 MHz at  $k_z = 0$  to 1.3352 MHz at  $k_z = 20$ . Higher  $k_z$ values indicate a more percentage of epoxy in material gradation composition, which lowers stiffness and thus reduces the natural frequency. In summary, increasing thickness h, higher content of  $CoFe_2O_4$ , and larger power-law index  $k_z$  all contribute to lower natural frequencies. These parameters offer tunability in the design of microbeam resonators by adjusting stiffness through material composition and geometric factors.

## CONCLUSION

In this study, we investigated the static bending and free vibration behavior of a bilaterally coated magneto-electro-elastic (MEE) microbeam using a quasi-3D high-order beam theory in conjunction with the Differential Quadrature Finite Element Method (DQ-FEM). The incorporation of the modified couple stress theory (MCST) effectively accounted for the microstructural effects within the beam. Our model, validated against existing literature, demonstrated a high degree of accuracy in predicting both the deflection and vibrational behavior of the microbeam under various loading and boundary conditions.

Beam thickness plays a significant role in reducing both midspan deflection and the magnitudes of electric and magnetic potentials, as thicker beams are stiffer and resist deformation.

Material composition influences the beam's response significantly. Higher proportions of BaTiO<sub>3</sub> increase the piezoelectric effect, enhancing both deflection and electric potential, while increased CoFe<sub>2</sub>O<sub>4</sub> improves the magnetostrictive response, raising the magnetic potential.

Material gradation affects the mechanical and electromechanical responses, with optimized combinations of BaTiO<sub>3</sub> -CoFe<sub>2</sub>O<sub>4</sub> and epoxy producing the highest electric and magnetic

Natural frequency decreases with both increasing beam thickness and the gradation index, indicating that the mechanical and vibrational properties are highly sensitive to material distribution.

These results highlight the importance of beam geometry and material composition in the design and optimization of MEE microbeams for applications that require precise control of mechanical, electrical, and magnetic responses. The developed model and numerical approach provide a robust framework for further exploration of functionally graded materials in micro-scale systems.

A comparative analysis between the MCST-based model and the classical model revealed that the couple stress effect introduces additional material stiffness at the microscale, leading to consistently lower deflections and energy potentials in the current model. The discrepancy between the two models becomes more pronounced as beam thickness decreases, emphasizing the significance of size-dependent effects in micro-scale systems. The results also show that increasing the length-to-thickness ratio enhances deflection, thereby increasing both electrical and magnetic potentials. However, this increase in flexibility also leads to a

reduction in natural frequencies due to the lower stiffness of thinner microbeams.

These results highlight the importance of beam geometry and material composition in the design and optimization of MEE microbeams for applications requiring precise control of mechanical, electrical, and magnetic responses. The developed model and numerical approach provide a robust framework for further exploration of functionally graded materials in micro-scale systems.

## 5. ANNEX

$$\begin{bmatrix} [K^e]_{11} &= I_1 \left[ Q^T A^{1^T} C A^1 Q \right] & [K^e]_{12} &= -I_2 \left[ Q^T A^{1^T} C A^2 Q \right] \\ [K^e]_{13} &= -I_3 \left[ Q^T A^{1^T} C Q^2 Q \right] & [K^e]_{14} &= I_8 \left[ Q^T A^{1^T} C Q \right] \\ [K^e]_{15} &= I_{14} \left[ Q^T A^{1^T} C Q \right] & [K^e]_{16} &= I_{17} \left[ Q^T A^{1^T} C Q \right] \\ [K^e]_{22} &= (I_5 + 4D_4) \left[ Q^T A^{2^T} C A^2 Q \right] \\ [K^e]_{23} &= (I_4 + 2D_5) \left[ Q^T A^{2^T} C A^2 Q \right] \\ [K^e]_{24} &= -I_9 \left[ Q^T A^{2^T} C Q \right] + 2D_6 \left[ Q^T A^{2^T} C A^2 Q \right] \\ [K^e]_{25} &= -I_{15} \left[ Q^T A^{2^T} C Q \right] \\ [K^e]_{33} &= (I_6 + D_8) \left[ Q^T A^{2^T} C A^2 Q \right] + (I_{11} + D_1) \left[ Q^T A^{1^T} C A^1 Q \right] \\ [K^e]_{34} &= -I_{10} \left[ Q^T A^{2^T} C Q \right] + (I_{13} + D_3) \left[ Q^T A^{1^T} C A^1 Q \right] + D_7 \left[ Q^T A^{2^T} C A^2 Q \right] \\ [K^e]_{35} &= -I_{16} \left[ Q^T A^{2^T} C Q \right] - I_{20} \left[ Q^T A^{1^T} C A^1 Q \right] \\ [K^e]_{36} &= -I_{19} \left[ Q^T A^{2^T} C Q \right] - I_{21} \left[ Q^T A^{1^T} C A^1 Q \right] \\ [K^e]_{44} &= I_7 [Q^T C Q] + (I_{12} + D_2) \left[ Q^T A^{1^T} C A^1 Q \right] + D_9 \left[ Q^T A^{2^T} C A^2 Q \right] \\ [K^e]_{45} &= -I_{22} \left[ Q^T A^{1^T} C A^1 Q \right] + I_{24} [Q^T C Q] \\ [K^e]_{55} &= -I_{26} \left[ Q^T A^{1^T} C A^1 Q \right] - I_{29} [Q^T C Q] \\ [K^e]_{56} &= -I_{28} \left[ Q^T A^{1^T} C A^1 Q \right] - I_{31} [Q^T C Q] \\ [K^e]_{66} &= -I_{27} \left[ Q^T A^{1^T} C A^1 Q \right] - I_{30} [Q^T C Q] \\ [K^e]_{66} &= -I_{27} \left[ Q^T A^{1^T} C A^1 Q \right] - I_{30} [Q^T C Q] \right]$$

$$\begin{cases}
[M^e]_{11} = J_1[Q^T \bar{C}Q] & [M^e]_{12} = -J_2[Q^T \bar{C}\bar{A}^1Q] \\
[M^e]_{13} = -J_3[Q^T \bar{C}\bar{A}^1Q] \\
[M^e]_{22} = J_1[Q^T \bar{C}Q] + J_5[Q^T \bar{A}^{1T} \bar{C}\bar{A}^1Q] \\
[M^e]_{23} = J_1[Q^T \bar{C}Q] + J_4[Q^T \bar{A}^{1T} \bar{C}\bar{A}^1Q] \\
[M^e]_{24} = J_8[Q^T CQ] \\
[M^e]_{33} = J_1[Q^T \bar{C}Q] + J_6[Q^T \bar{A}^{1T} \bar{C}\bar{A}^1Q] \\
[M^e]_{34} = J_8[Q^T CQ] \\
[M^e]_{44} = J_7[Q^T CQ]
\end{cases}$$
(36)

$$\begin{cases}
[F^e]_{22} = q_0[Q^T \bar{C}] \\
[F^e]_{33} = q_0[Q^T \bar{C}] \\
[F^e]_{44} = q_0[Q^T \bar{C}]
\end{cases}$$
(37)

All types of nodal arrangement for differentiation and quadrature reside inside the interval [-1, 1]. Consequently, to implement them in practice, the subsequent adjustments must be applied to the differential and quadrature matrices,

$$\bar{C} = \frac{l_e}{2}C, \quad \bar{A}^1 = \frac{2}{l_e}A^1, \quad \bar{A}^2 = \frac{4}{l_e^2}A^2$$
 (38)

Were  $l_e$  is the length of the microbeam element.

## **REFERENCES**

- Sahmani S, Aghdam MM. Nonlocal strain gradient shell model for axial buckling and postbuckling analysis of magneto-electro-elastic composite nanoshells. Composites Part B: Engineering. 2018;132:258-74. Available from: https://www.sciencedirect.com/science/article/pii/S1359836817312209.
- Farajpour MR, Shahidi AR, Hadi A, Farajpour A. Influence of initial edge displacement on the nonlinear vibration, electrical and magnetic instabilities of magneto-electro-elastic nanofilms. Mechanics of Advanced Materials and Structures. 2019;26(17):1469-81. Available from: https://doi.org/10.1080/15376494.2018.1432820
- Yakhno VG. An explicit formula for modeling wave propagation in magneto-electro-elastic materials. Journal of Electromagnetic Waves and Applications. 2018;32(7):899-912.

Available from: https://doi.org/10.1080/09205071.2017.1410076

- Haghgoo M, Hassanzadeh-Aghdam M-K, Ansari R. Effect of piezoelectric interphase on the effective magneto-electro-elastic properties of three-phase smart composites: A micromechanical study. Mechanics of Advanced Materials and Structures. 2019;26(23):1935-50. Available from: https://doi.org/10.1080/15376494.2018.1455932
- Chen W, Yan Z, Wang L. On mechanics of functionally graded hardmagnetic soft beams. International Journal of Engineering Science. 2020;157:103391. Available from: https://www.sciencedirect.com/science/article/pii/S0020722520301786
- Taati E. On buckling and post-buckling behavior of functionally graded micro-beams in thermal environment. International Journal of Engineering Science. 2018;128:63-78. Available from: https://www.sciencedirect.com/science/article/pii/S0020722518302489
- Dahmane M, Benadouda M, Fellah A, Saimi A, Hassen AA, Bensaid I. Porosities-dependent wave propagation in bi-directional functionally graded cantilever beam with higher-order shear model. Mechanics of Advanced Materials and Structures.

Available from: https://doi.org/10.1080/15376494.2023.2253546

- Khaje Khabaz M, Eftekhari SA, Hashemian M, Toghraie D. Optimal vibration control of multi-layer micro-beams actuated by piezoelectric layer based on modified couple stress and surface stress elasticity theories. Physica A: Statistical Mechanics and its Applications. 2020;546:123998. Available from: https://www.sciencedirect.com/science/article/pii/S0378437119322137
- Bhangale RK, Ganesan N. Free vibration of simply supported functionally graded and layered magneto-electro-elastic plates by finite element method. Journal of Sound and Vibration. 2006;294(4):1016-38.
   Available from: https://www.sciencedirect.com/science/article/pii/S0022460X06000320
- Sladek J, Sladek V, Krahulec S, Chen CS, Young DL. Analyses of Circular Magnetoelectroelastic Plates with Functionally Graded Material Properties. Mechanics of Advanced Materials and Structures. 2015;22(6):479-89.

Available from: https://doi.org/10.1080/15376494.2013.807448

- Mahesh V. Porosity effect on the nonlinear deflection of functionally graded magneto-electro-elastic smart shells under combined loading. Mechanics of Advanced Materials and Structures. 2022;29(19):2707-25. Available from: https://doi.org/10.1080/15376494.2021.1875086
- Zhang GY, Qu YL, Gao XL, Jin F. A transversely isotropic magnetoelectro-elastic Timoshenko beam model incorporating microstructure and foundation effects. Mechanics of Materials. 2020;149:103412. Available from: https://www.sciencedirect.com/science/article/pii/S0167663620301137
- Hong J, Wang S, Zhang G, Mi C. On the Bending and Vibration Analysis of Functionally Graded Magneto-Electro-Elastic Timoshenko Microbeams. Crystals. 2021;11(10):1206.
   Available from: https://www.mdpi.com/2073-4352/11/10/1206
- Hong J, Wang S, Qiu X, Zhang G. Bending and Wave Propagation Analysis of Magneto-Electro-Elastic Functionally Graded Porous Microbeams. Crystals. 2022;12(5):732.
   Available from: https://doi.org/10.3390/cryst12050732
- 15. Qu YL, Li P, Zhang GY, Jin F, Gao XL. A microstructure-dependent



Besma Khouani, Ahmed Saimi, Ismail Bensaid

Bending and Vibration Analysis of Magneto-Electro Bilaterally Coated Quasi-3D Microbeam via DQ-FEM

- anisotropic magneto-electro-elastic Mindlin plate model based on an extended modified couple stress theory. Acta Mechanica. 2020;231(10):4323-50.
- Available from: https://doi.org/10.1007/s00707-020-02745-0
- Wang S, Hong J, Gu S, Xiao Z, Zhang G. A size-dependent isogeometric model for magneto-electro-elastic graded curved beams in advanced structures. Composite Structures. 2025;358:118877. Available from: https://doi.org/10.1016/j.compstruct.2025.118877
- Zheng Y-f, Qu D-y, Liu L-c, Chen C-p. Size-dependent nonlinear bending analysis of nonlocal magneto-electro-elastic laminated nanobeams resting on elastic foundation. International Journal of Non-Linear Mechanics. 2023;148:104255. Available from: https://www.sciencedirect.com/science/article/pii/S0020746222002256.
- Alibeigi B, Tadi Beni Y, Mehralian F. On the thermal buckling of magneto-electro-elastic piezoelectric nanobeams. The European Physical Journal Plus. 2018;133(3):133.
  - Available from: https://doi.org/10.1140/epjp/i2018-11954-7
- Ghobadi A, Beni YT, Golestanian H. Nonlinear thermo-electromechanical vibration analysis of size-dependent functionally graded flexoelectric nano-plate exposed magnetic field. Archive of Applied Mechanics. 2020;90(9):2025-70. Available from: https://doi.org/10.1007/s00419-020-01708-0
- Zheng Y-f, Zhou Y, Wang F, Chen C-p. Nonlinear deformation analysis of magneto-electro-elastic nanobeams resting on elastic foundation by using nonlocal modified couple stress theory. European Journal of Mechanics - A/Solids. 2024;103:105158. Available from: https://www.sciencedirect.com/science/article/pii/S0997753823002504
- Habibi B, Beni YT, Mehralian F. Free vibration of magneto-electroelastic nanobeams based on modified couple stress theory in thermal environment. Mechanics of Advanced Materials and Structures. 2019;26(7):601-13.
  - Available from: https://doi.org/10.1080/15376494.2017.1410902
- Alibeigi B, Tadi Beni Y. On the size-dependent magneto/electromechanical buckling of nanobeams. The European Physical Journal Plus. 2018;133(10):398. Available from: https://doi.org/10.1140/epjp/i2018-12208-6
- Zheng Y-f, Liu L-C, Qu D-y, Chen C-p. Nonlinear postbuckling analysis of magneto-electro-thermo-elastic laminated microbeams based on modified couple stress theory. Applied Mathematical Modelling. 2023;118:89-106. Available from: https://www.sciencedirect.com/science/article/pii/S0307904X23000227
- Fattaheian Dehkordi S, Tadi Beni Y. Size-dependent continuum-based model of a truncated flexoelectric/flexomagnetic functionally graded conical nano/microshells. Applied Physics A. 2022;128(4):320. Available from: https://doi.org/10.1007/s00339-022-05386-3
- Lyu Z, Ma M. Nonlinear dynamic modeling of geometrically imperfect magneto-electro-elastic nanobeam made of functionally graded material. Thin-Walled Structures. 2023;191:111004. Available from: https://www.sciencedirect.com/science/article/pii/S0263823123004822
- Wang S, Hong J, Wei D, Zhang G. Bending and wave propagation analysis of axially functionally graded beams based on a reformulated strain gradient elasticity theory. Applied Mathematics and Mechanics. 2023;44(10):1803-20. Available from: https://doi.org/10.1007/s10483-023-3042-6.
- Wang S, Hong J, Yin S, Zhang G. Isogeometric analysis of magnetoelectro-elastic functionally graded Mindlin microplates. Thin-Walled Structures. 2024;198:111740. Available from: https://www.sciencedirect.com/science/article/pii/S0263823124001836
- Lam DCC, Yang F, Chong ACM, Wang J, Tong P. Experiments and theory in strain gradient elasticity. Journal of the Mechanics and Physics of Solids. 2003;51(8):1477-508. Available from: https://www.sciencedirect.com/science/article/pii/S002250960300053X
- McFarland AW, Colton JS. Role of material microstructure in plate stiffness with relevance to microcantilever sensors. Journal of Micromechanics and Microengineering. 2005;15(5):1060. Available from: https://dx.doi.org/10.1088/0960-1317/15/5/024
- 30. Toupin RA. Elastic materials with couple-stresses. Archive for Rational

- Mechanics and Analysis. 1962;11(1):385-414. Available from: https://doi.org/10.1007/BF00253945
- Mindlin RD. Influence of couple-stresses on stress concentrations. Experimental Mechanics. 1963;3(1):1-7.
   Available from: https://doi.org/10.1007/BF02327219
- Mindlin RD. Micro-structure in linear elasticity. Archive for Rational Mechanics and Analysis. 1964;16(1):51-78.
   Available from: https://doi.org/10.1007/BF00248490
- Mindlin RD, Eshel NN. On first strain-gradient theories in linear elasticity. International Journal of Solids and Structures. 1968;4(1):109-24.
- Available from: https://www.sciencedirect.com/science/arti-cle/pii/002076836890036X

  34. Polizzotto C. A hierarchy of simplified constitutive models within iso-
- Polizzotto C. A hierarchy of simplified constitutive models within isotropic strain gradient elasticity. European Journal of Mechanics A/Solids. 2017;61:92-109. Available from: https://www.sciencedirect.com/science/article/pii/S0997753816302145
- 35. B.S. Altan, E.C. Aifantis. On Some Aspects in the Special Theory of Gradient Elasticity. Journal of the Mechanical Behavior of Materials. 1997;8(3):231-82.
  - Available from: https://doi.org/10.1515/JMBM.1997.8.3.231
- Ebrahimi F, Barati MR. Vibration analysis of embedded biaxially loaded magneto-electrically actuated inhomogeneous nanoscale plates. Journal of Vibration and Control. 2018;24(16):3587-607.
   Available from: https://journals.sagepub.com/doi/abs/10.1177/1077546317708105
- Kiani A, Sheikhkhoshkar M, Jamalpoor A, Khanzadi M. Free vibration problem of embedded magneto-electro-thermo-elastic nanoplate made of functionally graded materials via nonlocal third-order shear deformation theory. Journal of Intelligent Material Systems and Structures. 2018;29(5):741-63.
  - Available from: https://jour-nals.sagepub.com/doi/abs/10.1177/1045389X17721034
- Liu H, Lv Z. Vibration performance evaluation of smart magneto-electro-elastic nanobeam with consideration of nanomaterial uncertainties. Journal of Intelligent Material Systems and Structures. 2019;30(18-19):2932-52.
  - Available from: https://journals.sagepub.com/doi/abs/10.1177/1045389X19873418
- Xiao W-s, Gao Y, Zhu H. Buckling and post-buckling of magneto-electro-thermo-elastic functionally graded porous nanobeams. Microsystem Technologies. 2019;25(6):2451-70.
   Available from: https://doi.org/10.1007/s00542-018-4145-2
- Lim CW, Zhang G, Reddy JN. A higher-order nonlocal elasticity and strain gradient theory and its applications in wave propagation. Journal of the Mechanics and Physics of Solids. 2015;78:298-313. Available from: https://www.sciencedirect.com/science/article/pii/S0022509615000320
- Şimşek M. Nonlinear free vibration of a functionally graded nanobeam using nonlocal strain gradient theory and a novel Hamiltonian approach. International Journal of Engineering Science. 2016;105:12-27. Available from: https://www.sciencedirect.com/science/article/pii/S0020722516300520
- Li X, Li L, Hu Y, Ding Z, Deng W. Bending, buckling and vibration of axially functionally graded beams based on nonlocal strain gradient theory. Composite Structures. 2017;165:250-65. Available from: https://www.sciencedirect.com/science/article/pii/S0263822316304974
- Nguyen T-K, Vo TP, Thai H-T. Static and free vibration of axially loaded functionally graded beams based on the first-order shear deformation theory. Composites Part B: Engineering. 2013;55:147-57. Available from: https://www.sciencedirect.com/science/article/pii/S1359836813003223
- 44. Li S-R, Batra RC. Relations between buckling loads of functionally graded Timoshenko and homogeneous Euler–Bernoulli beams. Composite Structures. 2013;95:5-9. Available from: https://www.sciencedirect.com/science/article/pii/S0263822312003558
- Nguyen T-K, Nguyen B-D. A new higher-order shear deformation theory for static, buckling and free vibration analysis of functionally graded

sandwich beams. Journal of Sandwich Structures & Materials. 2015;17(6):613-31.

Available from: https://journals.sagepub.com/doi/abs/10.1177/1099636215589237

- 46. Van Vinh P. Deflections, stresses and free vibration analysis of bifunctionally graded sandwich plates resting on Pasternak's elastic foundations via a hybrid quasi-3D theory. Mechanics Based Design of Structures and Machines. 2021:1-32.
  - Available from: https://doi.org/10.1080/15397734.2021.1894948
- Adhikari B, Singh BN. Dynamic response of functionally graded plates resting on two-parameter-based elastic foundation model using a quasi-3D theory. Mechanics Based Design of Structures and Machines. 2019;47(4):399-429.
  - Available from: https://doi.org/10.1080/15397734.2018.1555965
- Bensaid I, Saimi A. Dynamic investigation of functionally graded porous beams resting on viscoelastic foundation using generalised differential quadrature method. Australian Journal of Mechanical Engineering. 2022:1-20.
  - Available from: https://doi.org/10.1080/14484846.2021.2017115
- Ahmed S, Abdelhamid H, Ismail B, Ahmed F. An Differential Quadrature Finite Element and the Differential Quadrature Hierarchical Finite Element Methods for the Dynamics Analysis of on Board Shaft. European Journal of Computational Mechanics. 2021;29(4-6):303

  –44. Available from: https://journals.riverpublishers.com/index.php/EJCM/article/view/5999
- Houalef IE, Bensaid I, Saimi A, Cheikh A. An analysis of vibration and buckling behaviors of nano-composite beams reinforced with agglomerated carbon nanotubes via differential quadrature finite element method. Mechanics of Advanced Materials and Structures. 2023:1-19. Available from: https://doi.org/10.1080/15376494.2023.2185706
- Saimi A, Bensaid I, Houalef IE. Dynamic analysis of a porous microbeam model based on refined beam strain gradient theory via differential quadrature hierarchical finite element method. Advances in Materials Research. 2023;12(2):133-59.
- Saimi A, Bensaid I, Civalek Ö. A study on the crack presence effect on dynamical behaviour of bi-directional compositionally imperfect material graded micro beams. Composite Structures. 2023;316:117032. Available from: https://www.sciencedirect.com/science/article/pii/S0263822323003768
- 53. Saimi A, Bensaid I, Khouani B, Mazari MY, Houalef IE, Cheikh A. A Novel Differential Quadrature Galerkin Method for Dynamic and Stability Behaviour of Bi-directional Functionally Graded Porous Micro Beams. European Journal of Computational Mechanics. 2023;32(04):393-440. Available from: https://journals.riverpublishers.com/index.php/EJCM/article/view/23191
- 54. Tadi Beni Y. Size-dependent electromechanical bending, buckling,

- and free vibration analysis of functionally graded piezoelectric nanobeams. Journal of Intelligent Material Systems and Structures. 2016;27(16):2199-215.
- Available from: https://jour-
- nals.sagepub.com/doi/abs/10.1177/1045389X15624798
- Tadi Beni Y. Size-dependent analysis of piezoelectric nanobeams including electro-mechanical coupling. Mechanics Research Communications. 2016;75:67-80. Available from: https://www.sciencedirect.com/science/article/pii/S0093641316300477
- Senthil VG, Vasundara VV, Vijay KV. A review and critique of theories for piezoelectric laminates. Smart Materials and Structures. 2000;9(1):24. Available from: https://dx.doi.org/10.1088/0964-1726/9/1/304
- Wang Q, Quek ST, Sun CT, Liu X. Analysis of piezoelectric coupled circular plate. Smart Materials and Structures. 2001;10(2):229. Available from: https://dx.doi.org/10.1088/0964-1726/10/2/308
- 58. Liu C, Liu B, Zhao L, Xing Y, Ma C, Li H. A differential quadrature hierarchical finite element method and its applications to vibration and bending of Mindlin plates with curvilinear domains. International Journal for Numerical Methods in Engineering. 2017;109(2):174-97. Available from: https://onlinelibrary.wiley.com/doi/abs/10.1002/nme.5277
- Li JY. Magnetoelectroelastic multi-inclusion and inhomogeneity problems and their applications in composite materials. International Journal of Engineering Science. 2000;38(18):1993-2011. Available from: https://www.sciencedirect.com/science/article/pii/S0020722500000148
- Zhang GY, Gao XL. Elastic wave propagation in 3-D periodic composites: Band gaps incorporating microstructure effects. Composite Structures. 2018;204:920-32. Available from: https://www.sciencedirect.com/science/article/pii/S0263822318318270

Besma Khouani: https://orcid.org/0009-0008-3096-2995

Ahmed Saimi: https://orcid.org/0000-0002-3722-2526

Ismail Bensaid: https://orcid.org/0000-0003-4316-0648



This work is licensed under the Creative Commons BY-NC-ND 4.0 license.